Imaging with Modular Linear Arrays of Cryogenic Nb Microbolometers**

E.N. Grossman[a], C.R. Dietlein[a,b], J.E. Bjarnason[a], M. Ramirez[b], M. Leivo[c],
J.A. Penttila[d], P. Helisto[c,] and A . Luukanen[e],

[a]NIST Optoelectronics Division, 325 Broadway, Boulder CO, CA, USA 80305
[b] Dept. of Electrical Engineering, Univ. of Colorado, Boulder, CO USA
[c] VTT Technical Research Center of Finland, Espoo Finland
[e]Millimeter-wave Laboratory of Finland, VTT, Espoo, Finland
[d]Aivon Oy, Espoo, Finland

ABSTRACT

We present ultrawideband imagery obtained with modular, 8-element, superconducting Nb microbolometer arrays. Conically scanned images are presented and compared with raster-scanned images obtained on the same arrays and from similar NbN arrays at VTT. Statistical data on detector non-uniformity, and methods for mitigating and compensating it are described. Low-noise readout is accomplished with room-temperature electronics using the transimpedance scheme of Pentilla et al. Characterization of spatial resolution, noise-equivalent temperature difference, and spectral response is done using metrology tools - standard targets, mm-wave blackbodies, and variable filters - that have been developed at NIST for this purpose.

Keywords: Microbolometer, terahertz, millimeter-wave, imaging

1. INTRODUCTION

The usefulness of mm-wave/terahertz (THz) imaging for detecting weapons or explosives concealed beneath clothing is well established[1], and a number of groups are developing practical systems to exploit this. Our approach is based upon a scanned linear array of cryogenic microbolometers. The microbolometers consist of superconducting hot-spot bolometers and have been well described before[2]. They are coupled to incident mm-wave/THz radiation through ultrawideband spiral antennas and a hyperhemispherical silicon substrate lens. The quasioptical nature of the coupling and the resistive impedance of the microbolometers provide an ultrawideband frequency response that is difficult to achieve with diodes or other highly reactive detector elements. We have already presented in previous papers examples of the imagery obtainable from a single-element detector of this type. We are presently developing a 128-channel camera based on these detectors. The readout system is based on the transimpedance amplifier approach of Pentilla[3] et al., which allows the readout electronics to be entirely room-temperature, without degrading the noise performance of the cyogenic detectors. Our approach to the scale-up of the focal plane is modular rather than monolithic. The focal plane is organized into 8-channel modules, each based on a single 8-element detector chip. We have constructed a simple 8-element imager based on a single module mounted in a small cryocooler. The present paper concentrates on two aspects of our scale-up to a large multichannel system. The first is detector uniformity, which was explored in the single-module system, and the second is the optical design for a full 128-channel system.

2. SINGLE-MODULE EXPERIMENTAL SETUP

---

* Contribution of the U.S. Government. not subject to copyright.

The single-module imager is cooled using a commercial Gifford-McMahon cryogenic refrigerator with a specified cooling power of 100 mW at 4 K. It achieves a base temperature slightly below 2.5 K. The cryostat surrounding the refrigerator was custom-built specifically for this purpose. Much of the geometry, both in this setup and in the full 128-channel imager, is set by the patterns of the lens-coupled spiral antennas. The combination of a planar antenna and substrate lens was first explored in general by Rutledge[4], and the particular use of hyperhemispherical lenses to maximize antenna gain was first described by Buettgenbach[5]. It results in an antenna beam that resembles that of a diffraction-limited aperture diameter is that of the substrate lens. That is, the pattern width scales inversely with frequency over an extremely broad band, limited in practice by the planar antenna. We have measured the patterns of our detectors using 4 mm substrate lenses at several frequencies[6], and based on those measurements, the 3dB beamwidths for the present detectors can be accurately parametrized as 9 THz-degrees/f, where f is the frequency.

2.1 IR filtering and thermal management

Because of the relatively wide beam of the lens-coupled antenna, the cryostat window and IR filters need to be relatively large. Our low-pass filters, mounted on the 65 K and 4 K stages, are comprised of a commercial expanded teflon foam (universally known by its trade name Zitex) whose mm-wave/THz transmission properties have been well characterized[7]. It is a relatively poor thermal conductor however, so absorbed IR radiation raises its temperature substantially above that of the stage to which it is mounted. This causes it to re-radiate within its IR stopband onto the lower temperature stages. It turns out that a total of three filter stages are required to reduce the IR load on the focal plane to a manageable level. The two that are mounted to the 65 K stage equilibrate (at their centers) at 215 K and 80 K, while that mounted to the 4 K stage equilibrates at 11 K. (These temperatures are directly measured in the single-module setup; very similar values are expected for the long, narrow filters designed for the large 128-channel system.)

For the same reasons, the heat-sinking of the detector die is very important. The module mounts physically support the detector die by pressing it between the Au-plated Cu traces of a conventional FR4 circuitboard and the Si substrate lens. The latter is accurately located by a photoetched stainless steel flexure, which provides the mechanical compliance needed for reliable electrical contact. The flexure however does not provide any significant heatsinking capability. Since the thermal resistance from the detector die to thermal ground through the circuitboard is nearly impossible to estimate theoretically with any confidence, we directly measured it. A Cernox chip thermometer was glued to a detector die, which was then mounted in the standard module with substrate lens, flexure, etc. The temperature rise resulting from applying a known bias power to a detector on the die, (i.e. using the detector as a heater), yielded a thermal resistance of approx. 250 μW/K. On the other hand, the temperature rise resulting from opening the cold filter apertures to radiation from the vacuum window was found to be 0.45 K, indicating a total radiative power absorbed on the die of approx 120 μW. This is completely consistent with an expected IR background load of ~ 60 μW/cm^2 in the focal plane (from the known temperatures and spectral transmittances of the Zitex filters) and the effective IR-absorbing area within a 25x25 mm module.

The largest single heat load for both the 8-channel and 128-channel systems is that due to the wiring to room temperature. Because of the large number of wires required in our non-multiplexed readout scheme, namely four per detector, this wiring constitutes a simple but critical element in the overall system design. We are using cable patterned from very thin, but otherwise ordinary, copper-on-Kapton flex circuitboard. The heat load is very difficult to predict a priori because of the unknown thermal conductivity vs. temperature profile for the particular Cu used on this circuitboard. We have measured this however, and find, for each 100 μm wide, 9 μm thick, and 45 cm long wire, a heat load from room temperature to T_{base}=2.5K of 110μW. These are bundled into (single-sided) 50-wire cables on 25 mm wide kapton substrates.

2.2 Microbolometer uniformity and sensitivity

A great many of the issues involved in scaling up a single-pixel detector technology to a practical multichannel imaging array have to do with detector uniformity. Relative calibration of detector gains in software, i.e. "flat-fielding", is ubiquitous in uncooled IR cameras, and in most other practical imaging technologies, but the amount of non-uniformity for which it can compensate is limited. Moreover, the human eye, and many automatic target recognition algorithms, are very sensitive to image artifacts due to residual detector non-uniformities, ("stripes" in common parlance). Although it was not apparent in our initial comparisons between Nb and NbN airbridge

bolometers[8], the most important tradeoff at present in our microbolometer technology is between sensitivity, which is superior in the Nb airbridges, and uniformity, which is clearly superior in the NbN devices (at least at present).
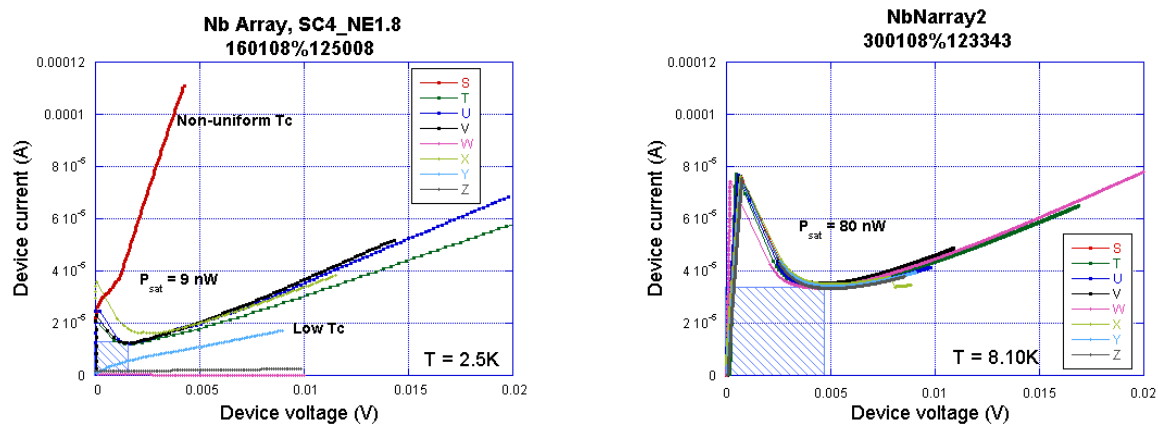
Fig. 1. Current-voltage characteristics of 8-element arrays of Nb (left) and NbN (right) microbolometers, displayed on the same scale. The normal-state resistance is manifested as the asymptotic slope at high bias.

This is well illustrated by current-voltage characteristics of the detectors in an 8-element module, shown in Fig. 1. The microbolometer dimensions have been designed to yield comparable normal-state resistances (R_n) for the two cases, and thus similar levels of impedance matching. However, there is a large difference in the electrical and thermal resistivities of the two materials. This leads to the Nb film being much thinner than the NbN, 30 nm vs 300 nm. The lower thickness is undoubtedly responsible for much of the difficulty in obtaining good uniformity. For example, the effect of unintentional surface oxidation between process steps on T_c is certainly much larger for a thinner film. Moreover, the difference in resisitivities also leads to a higher (longer and narrower) aspect ratio for the Nb bolometers than the NbN. This is turns tends to weight the frequency response of the NbN microbolometers toward higher frequency, since the upper frequency cutoff of the antenna is governed by the bolometer aspect ratio. As an illustration of the non-uniformities common within our current Nb arrays, on the particular 8-element Nb array in Fig. 1, two of the devices were burnt out by ESD during installation, a third displays a uniformly depressed critical temperature (T_c) compared to the others, and a fourth shows a depressed T_c along a portion of its length. The remaining four microbolometers show reasonably uniform R_n and saturation power (P_s), but the T_c on all of them is approx. 4K, about 2.5 K lower than on devices from other, nominally identical wafers. A depressed T_c on all or part of the microbolometer length does not necessarily preclude good THz response. Indeed, we have seen some evidence that noise and uniformity are actually improved when the T_c is closer to the base operating temperature[1]. However, it does require a much different bias point. Our electronics has therefore been modified to accommodate individual biasing for each microbolometer.

The advantage that accrues from the lower film thickness, as well as from the longer bridge length, of the Nb devices is a lower saturation power. P_s is manifested in the microbolometer I-V curves simply as half the total power dissipation of the device at its minimum current (indicated in Fig. 1 by the blue hatched rectangles). Detector responsivity scales as $P_S^{-1/2}$ and NEP and NETD scale as $P_S^{1/2}$, so the factor of approximately x9 in P_S translates into a substantial performance advantage on a single-pixel basis. Process changes to improve the uniformity of the Nb arrays, and mask changes to improve the saensitivity of the NbN arrays, are both underway.

3. OPTICAL DESIGN AND PERFORMANCE

In this section we describe the optical design and specifications for the full PEATCam system, and the optical design and performance of the 8-channel system used to acquire the images shown in section 4.

3.1 PEATCam system

The system design specifies a 2m x 4m field of view (FOV) at a target range of 8m. This constitutes an angular FOV of 14° x 28°, far larger than the FOV's typical for submillimeter telescopes intended for astronomical applications. Without correctors, the latter are typically limited to field diameters below one degree, and even with corrector systems, they cannot achieve field diameters above 3°[9]. The use of a conical scanner only partially mitigates this demand for a very wide field from the optics. We have therefore adopted a Schmidt optical design, which is the most common solution for very wide field telescopes. However, because of the extremely broadband frequency response, the system design is also specified to be completely reflective, thus eliminating the Schmidt telescope designs typically used in the optical region, which employ refractive corrector elements. All-reflective Schmidt telescopes were originally developed in the 1970's for the first ultraviolet space astronomy surveys[10, 11]. Because the corrector and the primary mirror are necessarily comparable in diameter, reflective Schmidt designs must be off-axis in order to avoid complete obscuration. This is actually an advantage for a practical mmwave/THz imager however, since the need to limit the system footprint strongly favors folded optical paths anyway. The figure of the corrector plate, a 6th-order polynomial in our case, is appropriately asymmetric in the two in-plane axes so as to compensate for the off-axis operation. A basic ray-trace diagram of the system optics is shown in the laft side of Fig. 2.

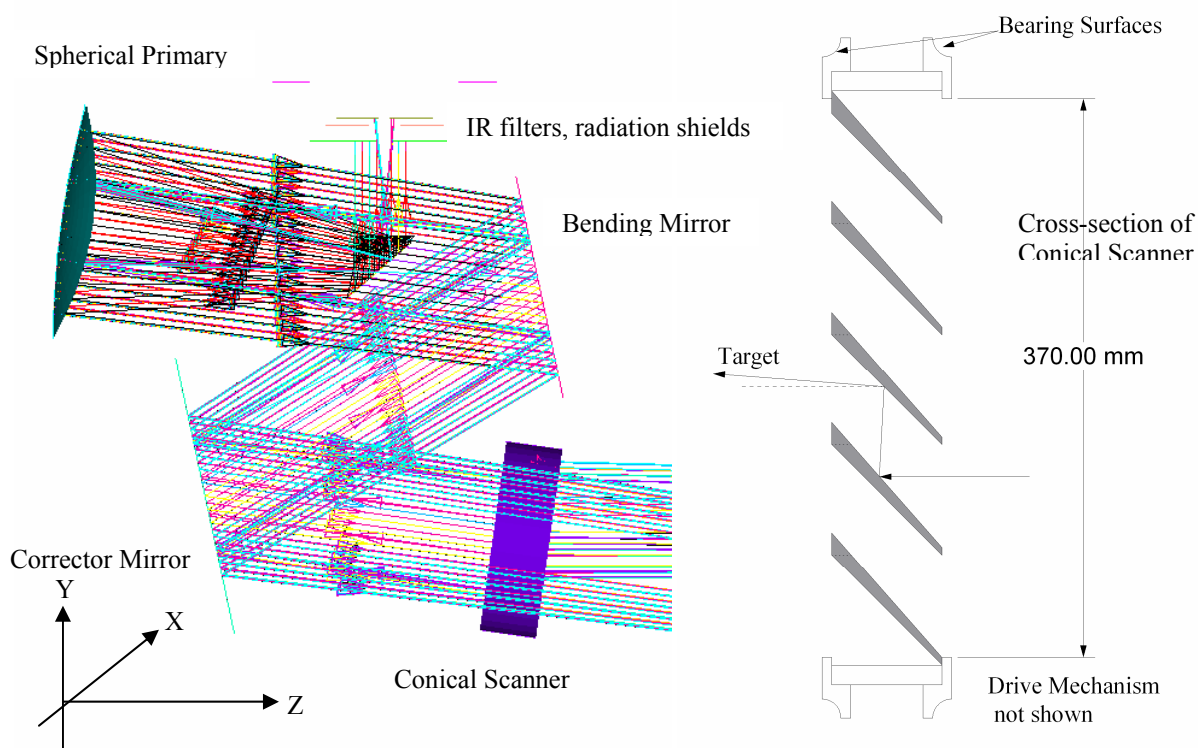---

[1] Luukanen,A., et al., this proceeding

Fig. 2 Scale drawing and ray-trace (left) of the PEATCam optics system. The linear array is oriented normal to the page, above the sequence of cryogenic radiation shields. (Right) Cross-section of the periscopic conical scanner.

The adopted design has only a single focusing mirror, the spherical primary.   The entrance pupil, which lies at the corrector plate, and coincides with the center of curvature of the primary, is rectangular. The conical scanner lies in front of (i.e. toward the target from) the entrance pupil, as close as possible without vignetting the ray bundle. The conical scanner employs a "periscopic" design that reflects each incident ray twice off a series of wedged vanes, once off the front of a vane and once off the back. The scanner is mounted and driven on its rim, eliminating any central obscuration due to axle-mounting. The entire system is rotated in the y-z plane so that light from the target enters the system at a nominal "lookdown angle" of 8°. This reflects the intended concept of operation for the imager – the imager is meant to be mounted somewhat higher than eye level, similar to a conventional video surveillance camera, and to survey people at the nominal range from a slightly elevated vantage point.

The reflective Schmidt geometry can accommodate a spherical secondary mirror (and further spherical focusing elements) if desired, and several intermediate versions of the design did incorporate a secondary mirror. However, the main performance limitation of the optics is not improved significantly by adding a secondary mirror, so it was eliminated. This performance limitation arises from the fact that three quantities, the system magnification, the antenna beamwidth, and the aperture size, were all effectively frozen by initial system design choices, even though their values are not completely compatible, and indeed cannot be completely compatible at all frequencies. The present design, in other words, constitutes a compromise. For a fixed aperture size, this compromise is between underfilling the antenna beam on the one hand, thereby losing efficiency, and making the magnification too large on the other, thereby reducing the sampling density (in the target plane) and degrading the spatial resolution. The addition of a secondary mirror allows one to improve one of these performance metrics at the expense of the other, but not to circumvent the tradeoff.

Fig. 3 illustrates the field-of-view in the target plane that results from this optical design. The magnification has been reduced so that the specified 4m x 2m FOV is covered by only the central 64 detectors of the array. The overall efficiency of the optics is approximately 29%. This is dominated by the efficiency of the conical scanner, which is approx. 55%, and the efficiency of the Schmidt optics, which is approximately 63%. The scanner efficiency in turn is dominated by vignetting of the edge vane and reflection off the flat surfaces at the front of the vanes. The efficiency of the Schmidt optics on the other hand is dominated by the obscuration of the final central bending mirror.
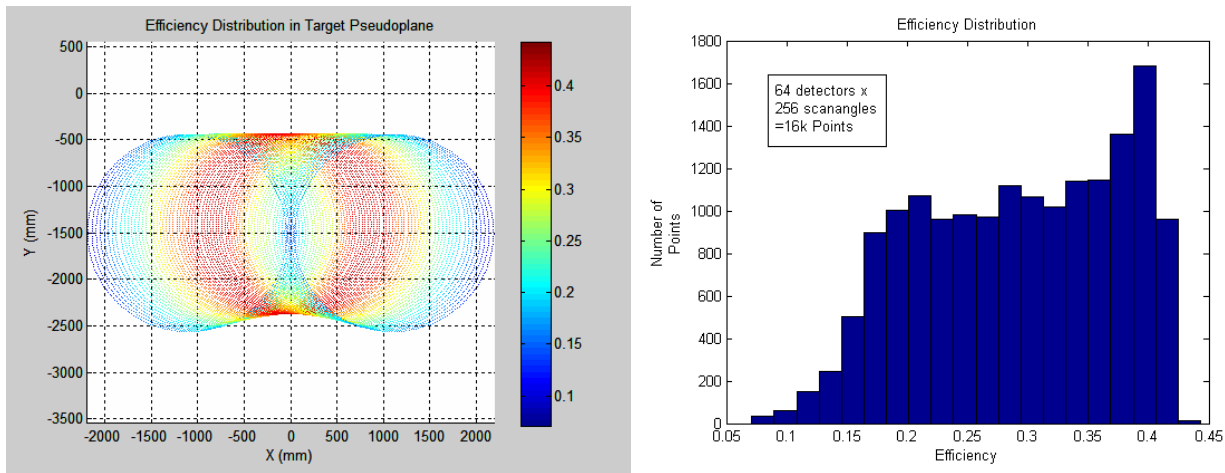

Fig. 3   Field-of view of the PEATCam optical system. (Right) Histogram of the overall optical efficiencies of the 16k pixels (64 detector x 256 scan angle) in the image. (Left) Distribution of the efficiency over the target plane.

An interesting feature of this optical system is that the deviation of the corrector plate from planar is actually quite small. The spherical aberration that it corrects is the dominant contributor to the geometric spotsize, but whether this geometric spotsize is greater or less than the diffraction-limited spotsize depends on the exact frequency within the 0.2-1.4 THz band of the focal plane array. We estimate that the corrector only improves the overall spotsize, which is the combination of aberration and diffraction induced components, at frequencies above 750 GHz, compared to a planar mirror. This is illustrated in Fig. 4, which compares the geometric spotsize distributions with the corrector and with a planar mirror in its place. This balance between aberration and diffraction-induced spotsizes does of course vary strongly as a function of range; the 750 GHz estimate and the distributions shown in Fig. 4 apply to the nominal 8 m range of the original design. It should also be noted that, although a planar mirror is far simpler conceptually than its 6-th order polynomial counterpart, for the sizes (~0.8 m on a side) and tolerances (~λ/20, or 15 μm at the top of the band) in question, planar mirrors and arbitrary near-planar figures are nearly identical in manufacturing difficulty and cost.
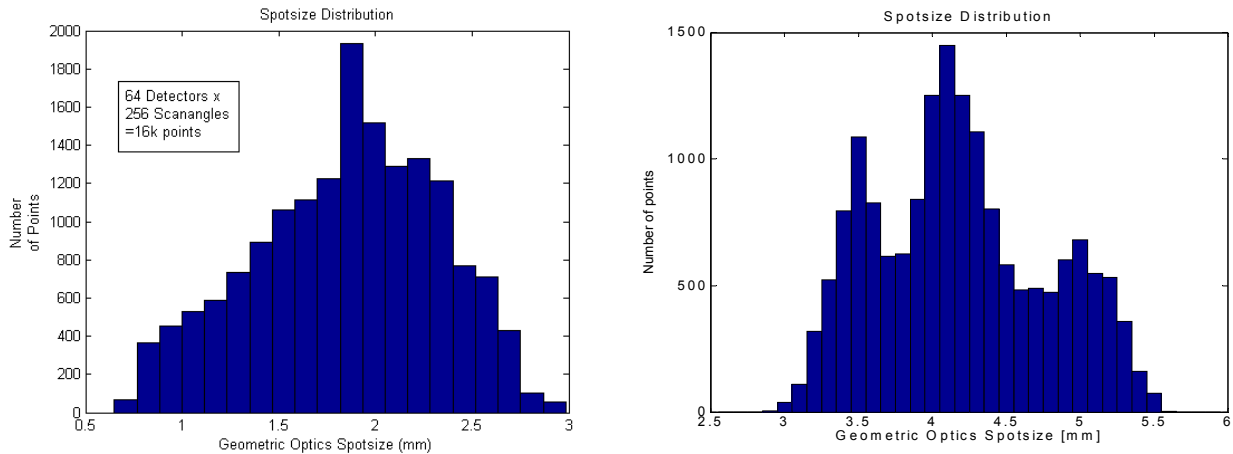
Fig. 4 Effect of the Schmidt corrector. Geometric spotsize distribution in the target plane for a 6th-order polynomial corrector (left) and a flat reflector (right).

4. IMAGERY FROM THE SINGLE-MODULE SETUP

The system described in Section 2, with a single 8-channel module cooled in a commercial closed-cycle refrigerator, has been incorporated into a simple imager that uses a 30 cm diameter spherical mirror off-axis to generate scanned images. Although its primary purpose is as a testbed for system integration of the modules, it can also produce images, and this is in fact an important part of the system integration, for example in developing algorithms or techniques for mitigating nonunifomrities in the detector gain.

One of our basic tools for tuning and characterizing the imaging performance is a calibrated THz blackbody that was especially developed for such purposes in a related DARPA program[12] and which we have described previously. The Aqueous Blackbody Calibration (ABC) source[13] provides an accurately known radiometric temperature over most of the imager's frequency band within a 20 x 20 cm aperture size. Images taken of the ABC source are shown in Fig. 5, and illustrate, through the sharpness of the source's edges, the spatial resolution and depth of field of the imager.
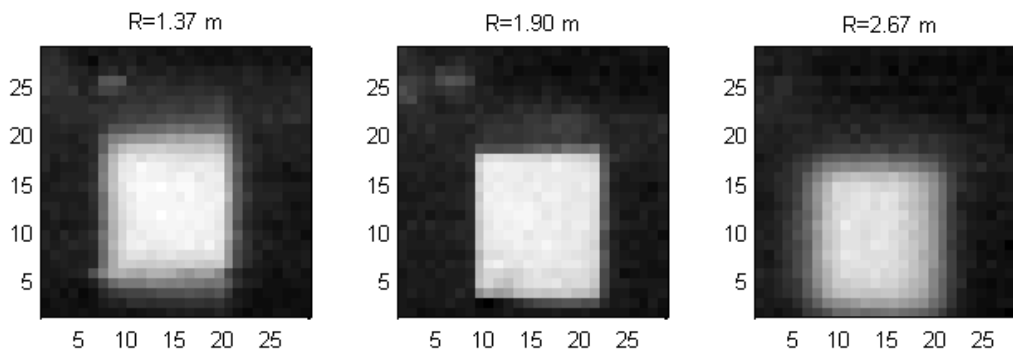

Fig. 5 Depth of field of the single-module imager. Images of the ABC source aperture at 3 different ranges (R=1.37 m, 1.90 m, and 2.67 m, left to right) with the focal plane array positioned so as to provide a nominal focus at R=1.88. The image is sampled at a spacing of 12 mm in the target plane in all cases. Only one of eight channels is shown.

Figure 6 illustrates the basic geometry of the imager. The dominant aberration of a spherical mirror used in the regime of small off-axis field angle and small aperture angle is astigmatism. If the entrance pupil, located at the

primary mirror in this case, is uniformly illuminated, then the rms blur diameter in the target plane is given by $s = (ROC)\sqrt{2m}\theta_1^2\theta_2$ where m is the magnification, and ROC the primary's radius of curvature.
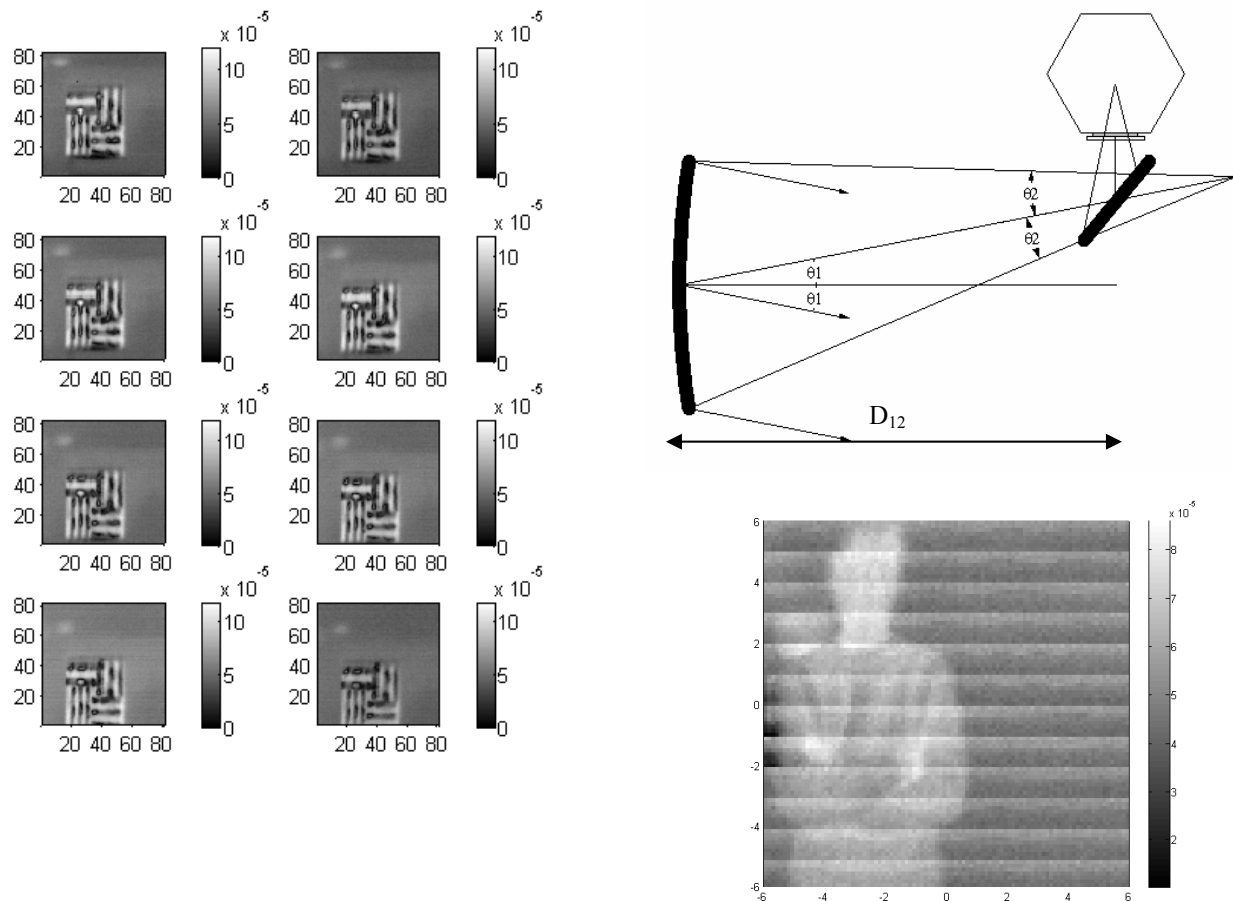

Fig. 6. Single-module imaging. (upper right) Basic geometry, illustrating field angle θ_1 and aperture angle θ_2. Adjustment of the distance D_{12} between primary and secondary focuses the system at varying target ranges. (left) Redundant imaging of the 8 channels on a resolution target positioned directly in front of the ABC aperture. Widths of target lines and spaces are, clockwise from upper left, 17 mm, 14mm, 13mm and 11 mm. (lower right) Non-redundant 8-channel image. Both images were taken at a target range of 1.9 m.

Figure 6 also illustrates a limitation of the flat-fielding that has been done for non-redundant imaging in this system. The relative gains of the channels were set by requiring the signal measured from each channel, when the array was focused on the ABC source aperture, to correspond to equal radiometric temperatures. It turns out that while this flattens the field at high signal levels (radiometric temperatures), it has the opposite effect at low signal levels, near the radiometric temperature of the background, i.e. room temperature. In other words, two parameters are required for each channel, a gain and an offset, in order to adequately flatten the field over the signal range of interest. We attribute this channel-dependent offset primarily to narcissus-effect, that is detection of the difference between the ambient temperature environment and the (colder) radiometric temperature presented to the detectors when the chopper blade reflects a small fraction of the radiation from the cryostat interior.

Figure 7 shows another redundant image set taken at much higher spatial sampling frequency in order illustrate the inherent spatial resolution capability of the setup. These images were taken with a NbN microbolometer array. (Note

the uniformity in brightness of the images, whose grayscales have all been set to cover the same global range.) As

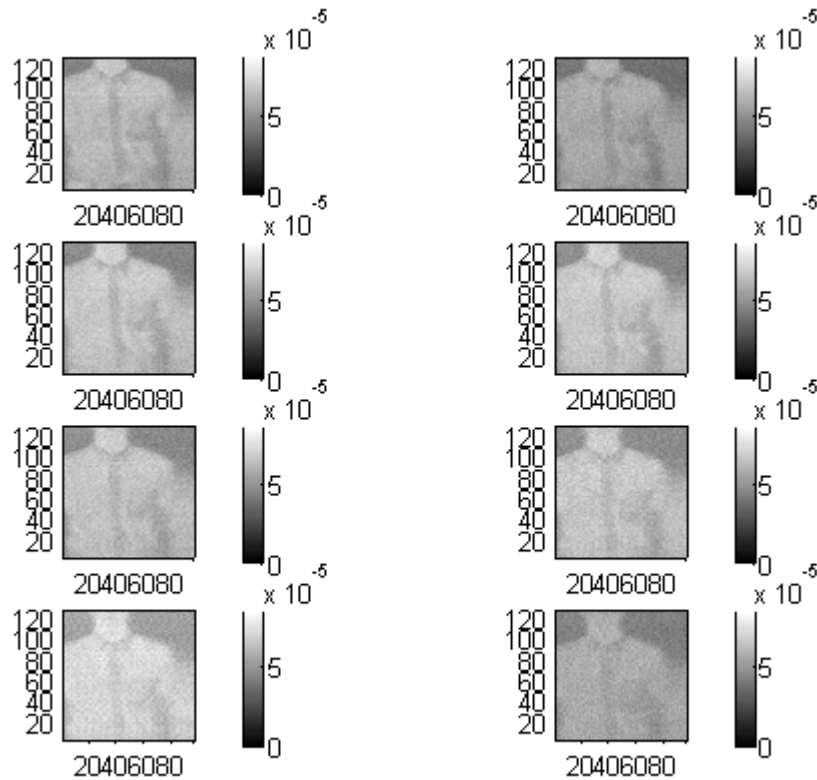Fig. 7. Redundant 8-channel imaging at the same 1.90 m range as in Fig.6, but at ~x3 higher spatial sampling frequency. A pair of reading glasses is located in the subject's breast pocket.

noted elsewhere[2], the frequency response is therefore weighted more heavily toward the higher frequency end of the nominal 0.2-1.5 THz band, with a corresponding decrease in penetration, as compared to other images taken with Nb microbolometers. The weakness of the signature from the reading glasses is a manifestation of this.

5. CONCLUSION

We have developed a modular 8-channel mm-wave/THz detector array and characterized it electrically and optically, in a small –scale cryocooled testbed. This is intended as a smaller-scale, but fully functional version of a complete 128-channel THz camera. Comparison of Nb and NbN microbolometer array dice indicate that the thinner Nb microbolometers provide better sensitivity, but the NbN devices provide superior uniformity. An optical design based on a Schmidt telescope and a periscopic conical scanner provides a nominal 2m x 4m FOV (14° x 28°) at a range of 8m, with approximately 30% optical efficiency and typical geometric spotsizes small enough that, at low mm-wave frequencies, overall spotsize will be limited by diffraction.

---

[2] Luukanen,A., et al., this proceeding

REFERENCES

[1]   R. Appleby, and Wallace, H.B., "Standoff Detection of Weapons and Contraband in the 100 GHz to 1 THz Region," *IEEE J. Anntennas and Propagation*, vol. 55, pp. 2944-2956, 2007.

[2]   A. Luukanen, Erich N. Grossman, Aaron J. Miller, Panu Helist¨o, Jari S. Penttil¨a, Hannu Sipola, and Heikki Sepp¨a, "An Ultra-Low Noise Superconducting Antenna-Coupled Microbolometer With a
Room-temperature Read-out," *IEEE Microwave and Wireless Components Letters* vol. 16, pp. 464-466, 2006.

[3]   J. S. Penttila, Sipola, H., Helisto, P., and Seppa, H., "Low-noise Readout of Superconducting Bolometers based on Electrothermal Feedback," *Superconductor Science and Technology*, vol. 19, pp. 319-322, 2006.

[4]   D. B. Rutledge, Neikirk, D. P., and Kasilingham, D. P., "Integrated Circuit Antennas," vol. 10, *Infrared and Millimeter Waves*, K. J. Button, Ed. New York: Academic Press, 1983, pp. 1-90.

[5]   T. H. Buettgenbach, "An Improved Solution for Integrated Array Optics in Quasi-optical Mm and Submm Receivers," *IEEE Trans. Microwave Theory and Tech..* vol. 41, pp. 1750-1761, 1993.

[6]   C. Dietlein, Chisum, J.D., Ramirez, M.D., Luukanen, A., Grossman, E.N., Popovic, Z., "Integrated Microbolometer Antenna Characterization from 95-650 GHz," *Intl. Microwave Symposium Digest*, pp. 1165-1168, 2007.

[7]   D. J. Benford, Gaidis, M., and Kooi, J.W., "Optical properties of Zitex in the Infrared to Submillimeter," *Appl. Optics*, vol. 42, pp. 5118-5122, 2003.

[8]   C. Dietlein, Luukanen, A., Pentilla, J.S., Sipola, H., Gronberg, L., Seppa, H., Helisto, P., and Grossman, E.N., "Performance Comparison of Nb and NbN Antenna-coupled Microbolometers," *Proc. SPIE*, vol. 6549, pp. 65490-M, 2007.

[9]   D. J. Schroeder, *Astronomical Optics*. San Diego: Academic Press, 1987.

[10]   D. Korsch, "Reflective Schmidt Corrector," *Applied Optics*, vol. 13, pp. 2005-2006, 1974.

[11]   D. J. Schroeder, "All-reflecting Baker-Schmidt Flat-field Telescopes," *Applied Optics*, vol. 17, pp. 141-144, 1978.

[12]   C. M. Stickley, Filipkowski, M., "Microantenna Arrays: Technology and Applications; MIATA an Overview," *Proc. 1st Eurpoean Symposium on Optics and Photonics in Security and Defence*, 2004.

[13]   C. Dietlein, Popovic, Z., and Grossman, E.N., "Broadband THz Aqueous Blackbody Calibration Source," *Proc. SPIE*, vol. 6549, 2007.